# UC Irvine

Title

Artificial Intelligence-based guidance of Image Reconstruction in Photo Magnetic Imaging

Permalink

https://escholarship.org/uc/item/50g4z2fn

Author

Pathare, Rajas Rajendra

Publication Date

2022

Peer reviewed|Thesis/dissertation

UNIVERSITY OF CALIFORNIA,
IRVINE

Artificial Intelligence-based guidance of Image Reconstruction
in Photo Magnetic Imaging

THESIS

submitted in partial satisfaction of the requirements
for the degree of

MASTER OF SCIENCE

in Electrical and Computer Engineering

by

Rajas Rajendra Pathare

Thesis Committee:
Associate Professor Gultekin Gulsen, Chair
Assistant Researcher Farouk Nouizi
Professor Terence Sanger
Professor Ozdal Boyraz

2022

# TABLE OF CONTENTS

# LIST OF FIGURES

# LIST OF TABLES

# ACKNOWLEDGEMENTS

# ABSTRACT OF THE THESIS

Artificial Intelligence-based guidance of Image Reconstruction

in Photo Magnetic Imaging

by

Rajas Rajendra Pathare

Master of Science in Electrical and Computer Engineering

University of California, Irvine, 2022

Associate Professor Gultekin Gulsen, Chair

Photo Magnetic Imaging is an imaging technique first proposed and created at the Center for Functional Onco Imaging at the University of California, Irvine. This imaging technique was first developed to early detect and identify cancerous regions in the biotissue using a combination of near-infrared laser-based optical imaging and Magnetic Resonance Thermometry (MRT) techniques. In PMI, the imaged tissue is illuminated and slightly warmed up with a near-infrared laser. The laser-induced temperature increase through absorption is measured using MRT. PMI absorption images are then obtained using a multiphysics solver combining light and heat propagation. This model is used to describe the spatiotemporal distribution of laser-induced temperature increase. Then, a dedicated PMI reconstruction algorithm is used to recover high-resolution optical absorption maps from temperature measurements. Being able to perform measurements at any point within the medium, PMI overcomes the limitations of conventional diffuse optical imaging. Higher absorption regions warm up more than the tissue background and thus can be directly seen on the MRT maps. These regions are observed as highly diffused bright blobs due to temperature diffusion. In fact, the boundaries of these regions are generally smaller

than these diffused blobs. Therefore, overcoming the diffusion effect and accurately detecting the real boundaries of these regions provides invaluable information about their location and size.

The focus of this research work is to provide a fast computational technique to employ novel machine learning techniques to perform the challenging aforementioned task. Here, we propose a Region-Based Convolutional Neural Network methodology in which the MRT temperature maps are first decomposed into square overlapping regions that cover the whole imaged medium. Then, Convolutional Neural Networks are used to classify these regions into 1) Positive, if they contain one of these diffused blobs, or 2) Negative, if not. Finally, a multi-regression model is used to identify the boundaries of these regions using an intersection over union of all the Positive square regions our method is tested and validated on a variety of cases with a mean accuracy of 95.35%.

# Chapter 1: Introduction

Medical imaging has witnessed several major developments to become an invaluable tool for the early diagnosis and treatment of cancer. It is mainly classified into two categories, anatomical and functional imaging.

Anatomical imaging is generally used to obtain critical structural information about the body and its internal organs. This structural information can also reveal various diseases depending on the interaction of different imaging techniques with the imaged tissue. This helps in detecting several diseases like cancer, cardiovascular disorders, neurological disorders, and many other medical conditions. Some of the commonly used imaging techniques include Computer Tomography (CT), Magnetic Resonance Imaging (MRI), X-rays, Ultrasound, etc.

Functional imaging (or physiological imaging) provides functional information such as changes in metabolism, blood flow, regional chemical composition, and absorption. Some of the techniques include Functional Magnetic Resonance Imaging (fMRI), Positron Emission Tomography (PET), Electroencephalography (EEG), and Diffuse Optical Imaging (DOI). The latter has recently seen major advancements allowing it to be a tool for the detection and diagnosis of different diseases including cancer. Optical imaging is capable of providing functional information similar to conventional imaging techniques without harming the patient as it utilizes non-ionizing light in the near-infrared spectral region (NIR).

## 1.1 Diffuse Optical Tomography (DOT)

Diffuse Optical Tomography (DOT) is an emerging optical imaging technique that provides functional information about biological tissue [1-5]. It utilizes the low attenuation near-infrared

(NIR) light to examine deep tissues by illuminating the imaged tissue from multiple locations. The incident light propagates through the tissues and is mainly affected by scattering and absorption resulting in attenuation of light intensity. This attenuated light is then detected and measured by multiple photodetectors at several points of its outer surface to generate tomographic images [6-13]. The photodetectors placed right beside the light source are used to measure the reflected light and on the opposite side to detect the transmitted light [14-16]. DOT image reconstruction algorithms recover the tissue's unknown optical properties by matching the measured data with a simulated one, which is generally obtained through modeling based on the diffusion equation [17-20].

DOT is an emerging imaging tool that can be employed for breast cancer monitoring [21-24], joint disease imaging such as rheumatoid arthritis [25], and functional brain imaging [6, 26]. DOT has the ability to image metabolic compounds such as water, lipid, oxy, and de-oxyhemoglobin [27-29]. Optical imaging can be used safely and frequently due to its non-ionizing nature of radiation and low cost [9, 12, 22].

Although DOT seems promising, it still has many limitations that have hindered its translation to the clinical arena. One of the limitations is the highly scattering nature of the biological tissues, which makes it extremely challenging to reconstruct good spatial resolution DOT images. Indeed, the ill-posed nature of the inverse problem and the non-uniqueness of its solution [30, 31] degrades the quantitative accuracy of DOT, which could lead to an inaccurate diagnosis of the disease and its treatment. Therefore, it is necessary to find a method that could provide more accurate and reliable functional information.

## 1.2 Photoacoustic Tomography (PAT)

Photoacoustic Tomography (PAT) is a biomedical imaging modality that leverages the spatial resolution of ultrasonic and the sensitivity of optical imaging [32]. PAT illuminates the biological tissues with laser pulses. Once absorbed by the tissue, the absorbed laser energy is converted into heat resulting in thermo-elastic expansion of the tissue. This expansion is responsible for the ultrasonic emission that is detected by ultrasonic transducers. Pat image reconstruction algorithms use these acoustic signals to obtain images of the tissue's absorption distribution. PAT allows to probe the tissue deeper than DOT due to the weak scattering of sound waves in the medium compared to light.

However, PAT also faces certain limitations in terms of image spatial resolution degradation. When probing deep tissues, the spatial resolution is degraded due to the absorption of shallow tissues. Hence, there exists a trade-off between spatial resolution and depth [33]. Some of the other drawbacks include acoustic impedance mismatch and transducer configuration. Acoustic impedance mismatch between tissues causes strong reflections. The arrangement of transducers plays an important role because arranging them in one line compromises the accuracy of the recovered image [34], whereas arranging them in a ring shape for better accuracy, would increase the complexity and cost [35].

## 1.3 Photo-Magnetic Imaging (PMI)

The Center for Functional Onco Imaging (CFOI) introduced a new alternative technique termed Photo-Magnetic Imaging (PMI) [36-38] to overcome the previous limitations and generate unprecedented high-resolution absorption images. PMI combines the NIR light and Magnetic

Resonance Thermometry (MRT) instead of Magnetic Resonance Imaging (MRI) for obtaining the structural *a priori* information as in multimodality conventional methods. It measures the internal spatiotemporal distribution of temperature variation induced by the absorption of light when the medium is illuminated by the light source. PMI generates simulated temperature maps by modeling light and heat propagation and diffusion in tissue [19, 38-52]. Modeling consists in solving the combined diffusion and Pennes' bioheat thermal equations using the Finite Element Method (FEM). A dedicated PMI reconstruction algorithm is used to recover the optical absorption maps by minimizing the difference between the measured and simulated spatiotemporal temperature maps. Being able to perform measurements internally makes the number of measurements and unknowns equal, which in turn makes PMI's inverse problem well-posed unlike DOT's. Thus, PMI provides absorption maps with high quantitative accuracy and spatial resolution.

The feasibility of PMI was successfully proved using the first prototype that allowed only a single-side illumination of the tissue. It was then upgraded to four-port illumination to offer a significantly higher signal-to-noise ratio (SNR) [39-44]. The new system allowed us to perform within the American National Standards Institute (ANSI) defined by the skin exposure limits. This new prototype is the first step towards the future clinical use of PMI for diagnosis.

## 1.4 Artificial Intelligence in PMI

To improve the spatial resolution of DOT, several research groups explored the possibility of incorporating high-resolution structural information, which is provided by anatomical imaging to guide the image reconstruction algorithm of DOT. This approach is widely known as reconstruction using a priori information [5, 16]. However, this approach systematically fails when the structural boundary does not match the functional information. Our group introduced a novel

4

concept, where functional a priori information is retrieved and then used to guide the image reconstruction process [16, 53-59]. In PMI, higher absorption regions warm up more than the tissue background and thus can be directly seen on the MRT maps. These regions are observed as highly diffused bright blobs due to temperature diffusion [38]. In fact, the boundaries of these regions are generally smaller than these diffused blobs. Therefore, overcoming the temperature diffusion effect and accurately detecting the real boundaries of these regions provides invaluable information about their location and size.

Machine learning techniques are a fast computational solution to retrieve the real boundaries of these higher absorption regions responsible for these bright temperature blobs. In this thesis, we propose a Region-Based Convolutional Neural Network methodology in which the MRT temperature maps are first decomposed into square overlapping regions that cover the whole imaged medium. Then, Convolutional Neural Networks are used to classify these regions. These square regions can be classified as "Positive" if they contain one of these diffused blobs, or "Negative" if not. Finally, a multi-regression model is used to identify the boundaries of these regions using an intersection over union of all the Positive square regions.

Once delineated, these regions are used to form a binary mask with ones inside the regions and zeros elsewhere. This binary mask is then used to construct a penalty matrix that will be used to constrain and guide the PMI image reconstruction algorithm [55, 60, 61].

# Chapter 2: PMI Reconstruction Algorithm

In PMI, a near-infrared (NIR) laser is used to illuminate the imaged medium in order to slightly increase its temperature [37, 38, 62]. The dedicated PMI reconstruction algorithm uses internally measured MRT maps within a medium to reconstruct high-resolution maps of its optical absorption. During the PMI image reconstruction, simulated temperature maps are generated by modeling the propagation of light and its corresponding light-absorption-induced temperature increase throughout the medium. This step, also known as the PMI forward problem, is generally performed using a finite element method (FEM)-based solver [38, 40-42, 44-49, 51, 52]. Then, the PMI reconstruction algorithm uses a gradient descent optimization method to minimize the difference between the measured maps and the simulated ones.

## 2.1 PMI forward problem

Solving the forward problem is performed in two steps, one modeling the laser light propagation, and the second modeling induced heat increase and propagation which are described as follows:

## 2.1.1 Modeling light propagation

In the first step, the diffusion equation [7-10, 12, 13, 19, 20, 23, 24, 31, 53, 56-59, 63-69] is used to model the propagation of light in the medium ($\Omega$). The diffusion equation allows us to calculate the density of photons $\Phi(r)$[W.mm$^{-2}$] at any position r [mm] using the spatial distribution of the absorption, $\mu_a$ [mm$^{-1}$], and the diffusion, D [mm], coefficients, respectively.

$$-\nabla D(r)\nabla\Phi(r) + \mu_a(r)\Phi(r) = q_0(r) \qquad (1)$$

where $q_0(r)$ is the isotropic source of light and $\mu'_s$ [mm$^{-1}$] is the reduced scattering coefficient.

The diffusion coefficient D is defined as:

$$D(r) = 1/[3(\mu_a + \mu'_s)] \tag{2}$$

The Newman boundary conditions are used to solve Eq. 1:

$$\underline{n}D\nabla\Phi(r) + A\Phi(r) = 0 \ \ (r \ \epsilon \ \delta\Omega) \tag{3}$$

where $\partial\Omega$ is the surface boundary, $\underline{n}$ is the vector normal to $\partial\Omega$, and A is the surface mismatch modeling coefficient [9].

## 2.1.2 Modeling heat propagation

In this step, the laser-induced temperature T [˚C] and its dynamics T(r,t) within the medium is modeled using Pennes bio-heat equation [19, 44, 47-50, 70, 71]. It is used to model the heat transfer in biological tissue as follows:

$$\rho c \frac{\partial T(r,t)}{\partial t} - \nabla k \nabla T(r,t) = \Phi(r)\mu_a(r) \tag{4}$$

where $\rho$ [g mm$^{-3}$] is the density, c [J (g ˚C)$^{-1}$] is the specific heat, and k [W (mm ˚C)$^{-1}$] is the thermal conductivity of the medium. The source of heat resulting from the laser light absorption by the medium is modeled by the product of the optical absorption and the photon density at any point within the medium as can be seen on the right-hand side of Eq. 4. Eq. 4 is solved using the heat convection boundary condition:

$$-k\frac{\partial T(r)}{\partial n} = h[T_f(r) - T(r)] \ \ (r \ \epsilon \ \delta\Omega) \tag{5}$$

which states that the heat transfer between medium and surrounding air having an ambient temperature $T_f$ [˚C] is a function of their temperature difference and heat transfer coefficient h [W $(mm^2$ ˚C$)^{-1}$]. For PMI, Eq. 4 represents the modified version of the Pennes bioheat equation to heat conduction equation [48, 66T]. This equation shows that the rate of heat energy flow due to conduction and the rate of heat energy generated by the laser at any time and position r in the medium is equal to the rate of heat energy accumulated in the medium. The terms of blood perfusion and heat generated by metabolism from the original bio-heat equation are neglected.

## 2.1.3 Finite Element Method (FEM)

To solve the combined diffusion and heat equations FEM is the commonly used technique that provides a fast and accurate numerical solution. In FEM, a mesh is generated over a volume of the same dimensions as the imaged medium. This volume is divided into small connected triangular elements. These elements are connected by vertices, which are commonly known as mesh nodes. In this work, all the meshes are generated using the Matlab® PDE toolbox.
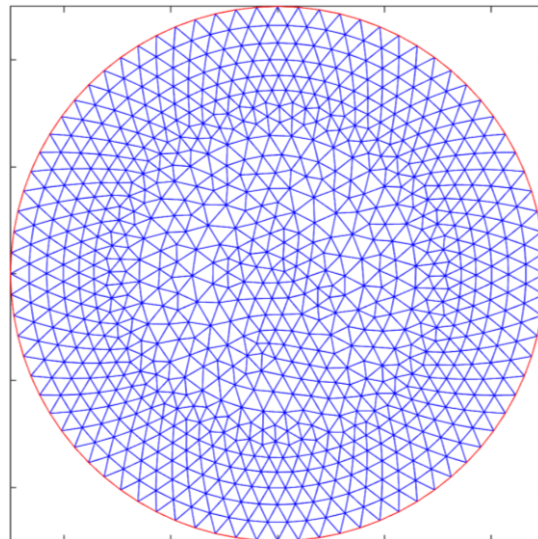


Figure 1: Representative FEM mesh.

## 2.2 PMI Inverse Problem

The solution to the PMI inverse problem recovers the optical absorption distribution at each node of the FEM mesh by minimizing the difference between the measured MRT temperature map ($T^m$) and the simulated temperature map [$T(\mu_a)$], which was obtained by resolving the forward problem as follows:

$$O(\mu_a) = \sum_{n=1}^{N} \left|\left| \text{T}^m{}_{s,d} - \text{T}_{s,d}(\mu_a) \right|\right|^2 \tag{6}$$

where N is the number of nodes in the FEM mesh. While minimizing the equation the unknown $\mu_a$ is iteratively updated using the Levenberg-Marquardt method by [72]:

$$\Delta\mu_a = (J^T J + \alpha I)^{-1} J^T [T^m - T(\mu_a)] \tag{7}$$

where $J$ is the Jacobian matrix, $\alpha$ is a regularization parameter, and $I$ is the identity matrix.

In the last decade, considerable work has been made to improve the spatial resolution of diffuse optical imaging. Briefly, the number of optical measurements is usually much smaller than the number of unknowns to be recovered. This makes the inverse problem highly ill-posed and under-determined, which results in the recovery of images with poor spatial resolution [31]. To overcome this limitation, several research groups successfully combined optical imaging with anatomical imaging techniques having drastically higher spatial resolution [14, 29, 61, 63, 64, 73-82]. In this approach, the update to the unknown $\mu_a$ is obtained as follow:

$$\Delta\mu_a = (J^T J + \alpha L^T L)^{-1} J^T [T^m - T(\mu_a)] \tag{8}$$

where *L* is a penalty matrix describing the binary mask retrieved from the anatomical structural information. This L penalty matrix is calculated as follows:

The penalty matrix L can be obtained as follows [53, 60, 83]:

$$L_{ij} = \begin{cases} 0 & \text{i and j not in the same region} \\ -\frac{1}{N_r} & \text{i and j in the same region} \\ 1 & i = j \end{cases} \tag{9}$$

where $N_r$ represents the number of nodes included in each region r. Unfortunately, this approach was also demonstrated to be limited due to the mismatch between the functional and structural information within the body. Therefore, our team at the Center for Functional Onco-Imaging-UCI introduced two novel methodologies that bring functional and anatomical imaging techniques to work synergically. These techniques termed Temperature Modulated Fluorescence Tomography (TMFT) [53, 55-59, 65, 66, 84-87] and PMI [38-49, 51, 52] utilize the anatomical imaging modality to induce or measure changes caused by the propagation of light within the medium. Thus, they are not limited to utilizing the anatomical information to only constrain their reconstruction algorithms. In PMI, which is the technique of interest in this work, information about the presence of higher absorbing regions can be directly extracted from the MRT-measured temperature maps before any reconstruction process. Unlike standard a priori anatomical information, these regions directly match the regions of interest to be later reconstructed by the PMI algorithm. However, due to temperature diffusion, the observed regions are diffused and are typically larger than the region to be reconstructed.

In this thesis, we utilize an AI-based algorithm that allows us to identify the real boundaries of these regions and overcome the limitation caused by temperature diffusion. The recovered

information will be converted to a binary mask that will be utilized to generate the penalty matrix using Eq. 9. The penalty matrix obtained using our new AI-based algorithm will be utilized to guide and constrain the PMI reconstruction algorithm as shown in Eq. 8 to retrieve the real high-resolution absorption coefficient of the medium.

# Chapter 3: Artificial Intelligence

## 3.1 Neural Networks

A neural network can be described as a machine specifically designed to replicate the way in which the brain processes any given data, extracts relevant information, and learns to perform any complex task. The learning is mainly done by cells referred to as "neurons".

Neural networks have several benefits such as non-linearity, which consists of their ability to understand non-linear data, and adaptivity, which is defined as the versatility of a neural network trained for some specific data that can be easily tweaked and retrained with some minor changes for completely different data.

As can be seen in Fig. 2, a neural network consists of four basic components, which are defined as follows:

1. Neuron: is the fundamental unit that does the processing in the network.

2. Set of synapses: are connecting links, which are characterized by a weight.

3. Adder: sums up the input signals with their respective weight of the synapses.

4. Activation Function: is generally a non-linear function used to limit the amplitude of the output neuron.
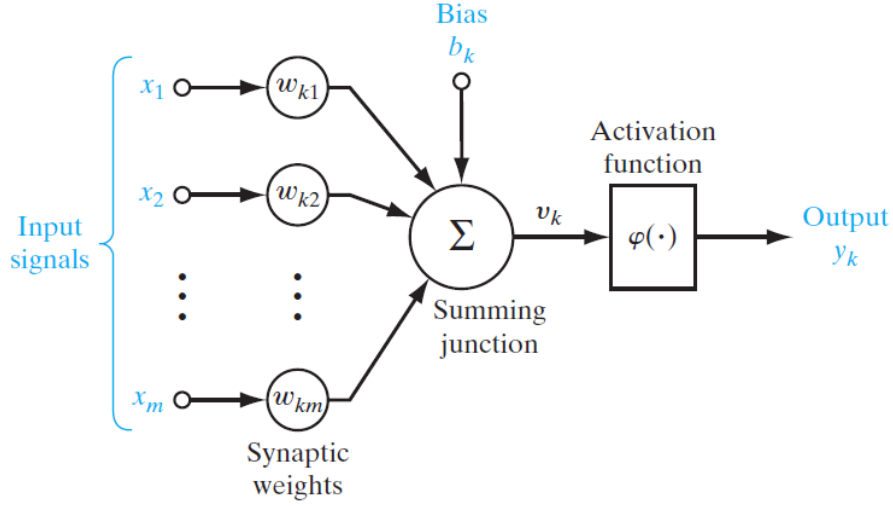
Figure 2: Representative schematic of the basic components of a neural network

Another important component in neural networks is bias. The bias is a parameter that increases or decreases the net output after the summation step.

$$u_k = \sum_{j=1}^{m} w_{kj} x_j \qquad (10)$$

and

$$v_k = u_k + b_k \qquad (11)$$

hence,

$$y_k = \varphi(v_k) \qquad (12)$$

where $x_1, x_2, \ldots, x_m$ are the input signals; $w_{k1}, w_{k2}, \ldots, w_{km}$ are the weights of synapses; $u_k$ is the summation of the input signals multiplied by their respective weights; $b_k$ is the bias; $\varphi(\cdot)$ is the activation function; and $y_k$ is the output signal of the neuron.

13

### 3.1.1 Forward Propagation

During forward propagation, the input data is propagated through the network in the forward direction and attempts to make predictions. Essentially, the weighted inputs to the neurons are summed up and processed as per the activation function and then passed onto the successive layer until the final layer gives the prediction. The next step is to minimize the error between the predicted output and the ground truth.

### 3.1.1.1 Activation Function:

An activation function $\varphi(.)$ is a mathematical function that adds non-linearity to the network required for learning. It determines the output of a neuron depending on the problem it is solving, e.g. if the problem is to predict two classes Sigmoid activation function can be used, whereas for multi-class classification we use Softmax. Some of the commonly used activation functions are as follows:

### 3.1.1.1.1 Sigmoid

The sigmoid activation function is a strictly increasing function and it is the most commonly used activation function, Fig. 3. It is defined by the logistic function:

$$\varphi(v) = \frac{1}{1 + e^{-av}} \tag{13}$$

where a is the slope of the function.
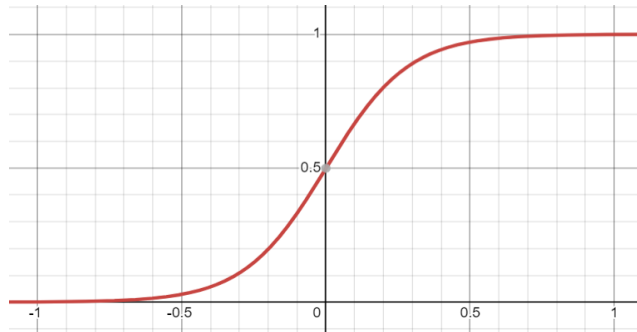
Figure 3: Graphical representation of Sigmoid.

## 3.1.1.1.2 Rectified Linear Units (ReLU)

The activation function needs to have non-linearity for it to support learning in the network. At first sight, ReLU looks like a linear function but it actually has a derivative function which makes that allows learning. Compared to other activation functions ReLU is very computationally efficient.

$$\varphi(v) \ = \ max(0, v) \tag{14}$$
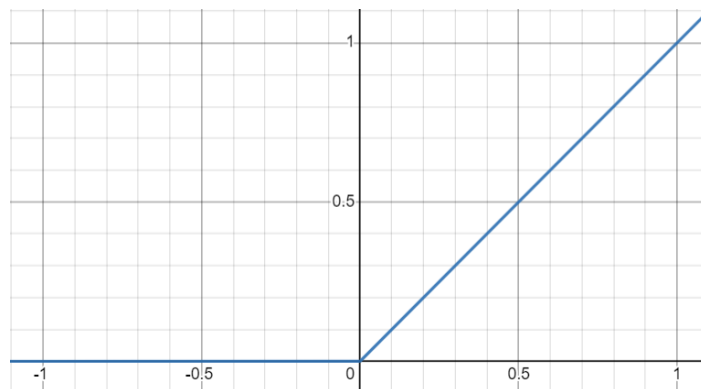


Figure 4: Graphical representation of ReLU.

### 3.1.1.1.3 Softmax

The softmax activation function is used in the last layer of a neural network which is trained for classifying more than two classes. It can be described as a combination of multiple sigmoid functions.

$$\varphi(v_i) = \frac{e^{z_i}}{\sum_j e^{z_j}} \tag{15}$$

### 3.1.2 Backward propagation

Backward propagation, commonly known as backpropagation, is an algorithm used to fine-tune the parameters, such as weights, and improve the overall prediction accuracy of the network. Basically, once the forward propagation is implemented and output is predicted it is compared with the ground truth using the loss functions which generates an error and this error needs to be minimized to improve the accuracy. This is achieved by calculating the gradient of the loss function at the output layer and propagating it backward to update the weights to minimize the loss function.

### 3.1.2.1 Loss Function

One of the important components which contributes significantly to the learning of neural networks is loss function. It can be defined as a method of evaluating how well the network is trained for a particular task. If the prediction is significantly different than the actual result, the loss function will return a large value. Therefore, training a neural network consists in iteratively minimizing the loss function until the predicted output matches the actual result.

### 3.1.2.1.1 Mean Squared Error

The mean squared error (MSE) is calculated by averaging the squared differences between predicted and actual outputs. It is a regression loss.

$$MSE = \frac{\sum_{k=1}^{n}(y_k - \widehat{y_k})^2}{n} \tag{16}$$

### 3.1.2.1.2 Cross-Entropy Loss

The cross-entropy loss is a metric that is mainly used while training the neural networks for classification. It is a classification loss.

$$CrossEntropyLoss = -(y_k log(\hat{y}_k) + (1 - y_k)log(1 - \hat{y}_k)) \tag{17}$$

## 3.2 Convolutional Neural Network (CNN)

CNN is a special type of neural network. It is a deep learning algorithm that focuses on the extraction of features from an image and learning based on summary statistics of the extracted features.

### 3.2.1 Components of CNN

The CNNs are composed of multiple components which are defined as follows:

### 3.2.1.1 The Input Layer

The first layer of the neural network is the input layer. The input layer feeds the input images to be processed by the model. For example, for RGB images the input would be a three-dimensional matrix.

## 3.2.1.2 The Convolutional Layer

The convolutional layer is responsible for encoding within its convolutions, spatial relationships between pixels in a given neighborhood. It is considered the most computationally expensive part of the neural network. This layer is generally used to extract spatial relationships between pixels of interest in specific regions of interest in the input training image. The output of this layer is a feature map that is injected directly into the next layer called the subsampling layer.
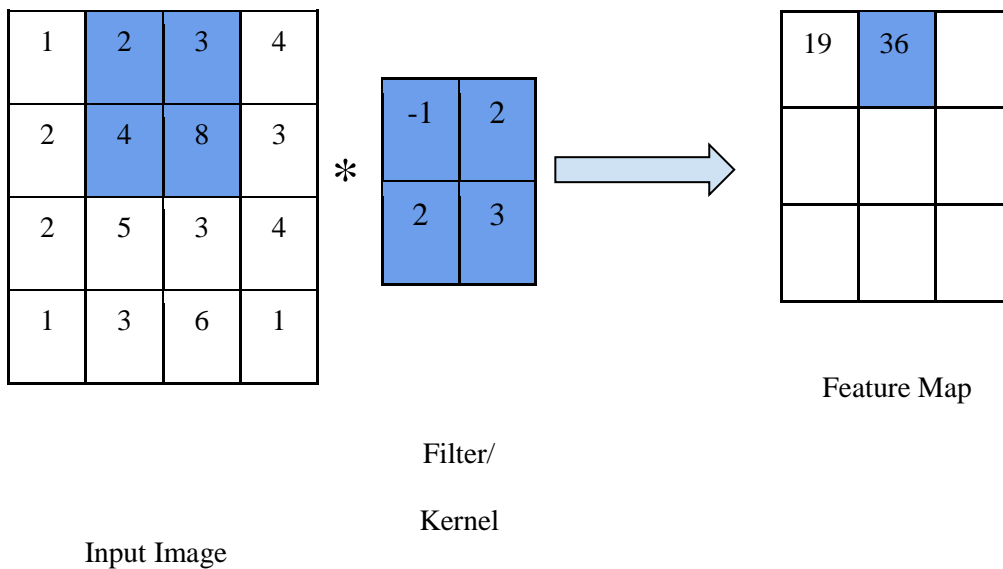


Figure 5: Schematic showing the principle of a kernel-based convolutional layer.

## 3.2.1.3 The Subsampling Layer

To reduce the spatial size of the feature map obtained by the convolutional layer, binning is performed. The final values of the reduced-size image are obtained by either an averaging or a maximum statistic of the binned pixels. In this paper, for this subsampling layer of the network,

we have used a *Max Pooling* method, which is a substitution with the maximum value of the region as can be seen in Fig. 6.
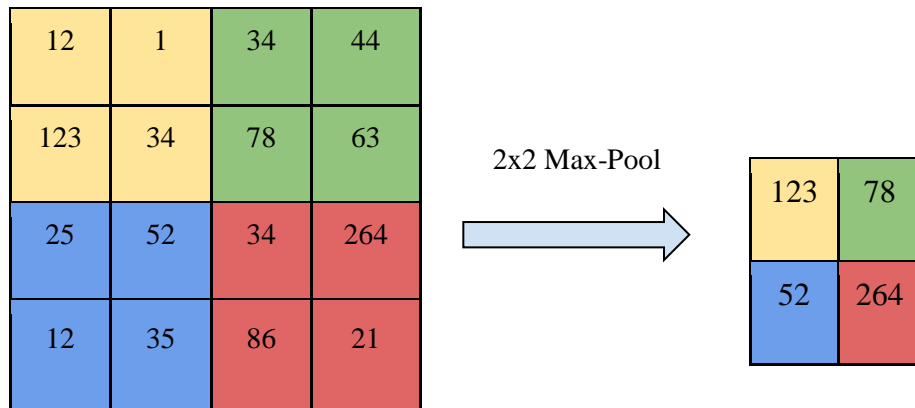


Figure 6: Schematic showing the principle of the max-pooling subsampling method.

## 3.2.2 Training in CNN
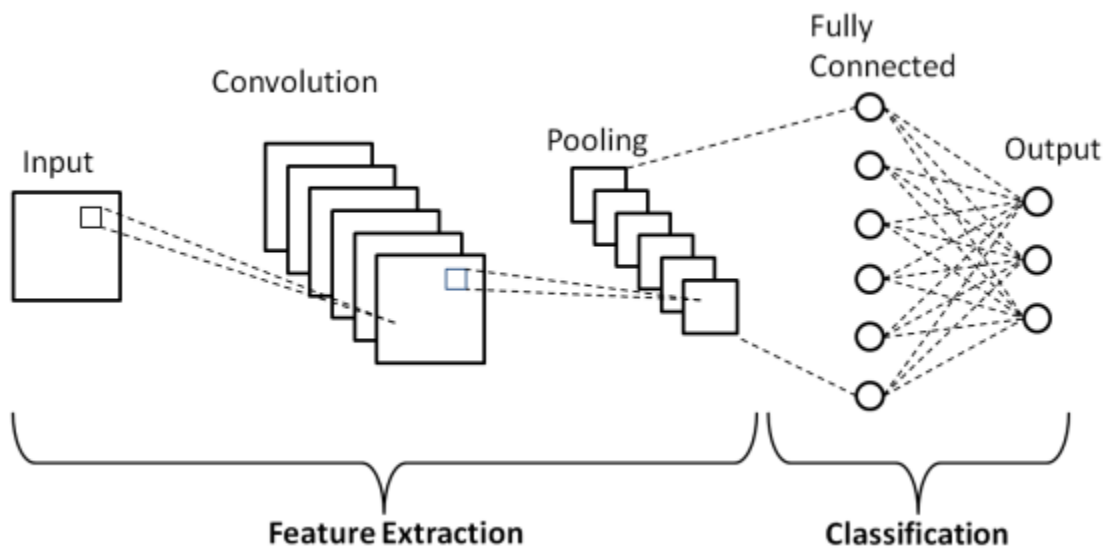


Figure 7: Schematic diagram of a basic convolutional neural network (CNN) architecture [64].

Like a standard neural network, CNN also has a two-phase architecture as described below:

### 3.2.2.1 The Forward Propagation in CNN

During the CNN forward propagation, a kernel or a square filter slides over the input image computing the convolution operation for each region that it overlaps with, producing a compact representation of the image, termed a *feature map*. Each convolutional layer of the network is composed of multiple feature maps. This is followed by the subsampling/pooling layer. These layers are repeated several times in sequence to maximize the power of the neural network for feature extraction. The output of each layer of the network is then passed to an activation function. This output is then compared with the actual expected output (ground truth) to compute the error.

### 3.2.2.2 The Backpropagation in CNN

The neural network learns by minimizing the error between the real output label (ground truth) and the predicted output obtained from the output layer. A loss function is then computed as a function of the errors obtained for a batch of training data. The most commonly used loss function for binary label classification purposes is the *Binary Cross Entropy* loss function.

During the minimization of the loss function, the error is then backpropagated throughout the network to adjust the learning parameters (synaptic weights) of the model using a gradient-based optimization method. One of the most powerful optimizers that is commonly used is the *Adam Optimizer*.

# Chapter 4: Methodology

This section describes the various procedures undertaken for the implementation of the Artificial Intelligence-based guidance to the PMI image reconstruction. Several methods were tried and implemented in this thesis, ranging from simple machine learning regression-based methods to more complex deep learning ideas, including the development of the final methodology adopted for PMI. The problem of reconstruction of the cancerous regions in the body of the phantom is two-fold. The first involves detection of the temperature diffused blobs in the temperature maps of the phantom that are assumed to correspond to tumors. The second part of reconstruction consists in the identification of the real boundaries of regions with high absorption that are responsible for the generation of these temperature blobs. Since the PMI image reconstruction algorithm is FEM-based, the last step of our method will map these real boundaries into the FEM mesh. This step allows to identify the nodes that belong to the high absorbing regions that will be recovered using the PMI reconstruction algorithm. Technically, this step consists in the so-called penalty matrix describing the a priori information, Eq. 8 and 9. In other words, the task for our novel AI-based algorithm consists in recognizing the nodes responsible for the formation of the diffused heat blobs on the MRT maps.

## 4.1 PMI Instrumentation
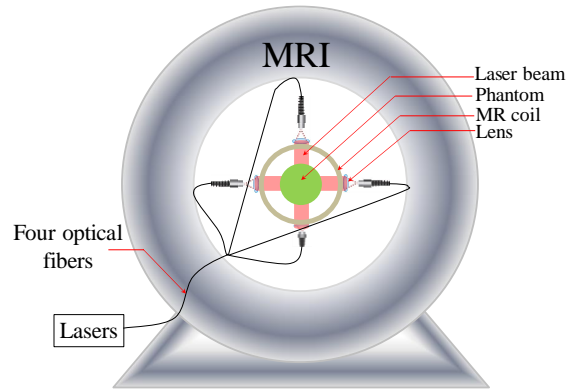
Figure 8: A schematic of the PMI setup showing the phantom and the optical instrumentation inside the MRI bore.

A Philips 3 Tesla Achieva system is used to acquire the MRT temperature maps. Phase maps are acquired using a gradient echo sequence using a 60 ms repetition time (TR) and 12 ms echo time (TE). The phantom is placed inside a home-built MRI coil paced within the MR bore, Fig 8. This imaging interface consists of a small animal dedicated RF coil having four windows, which permit illuminating the phantom from four sides. The phantom is illuminated using four laser diodes (808 nm, 7W, Focuslight, China). Four 15-meter-long optical fibers are used to transport the laser light from the laser system located in the control room to the PMI interface located inside the MR bore. For *in vivo* imaging, the laser power per unit area is set to the ANSI limits (0.32W/cm$^2$ for 808nm).

## 4.2 PMI Data Generation

In order to train our neural network model, a series of comprehensive simulated temperature maps have been generated. As discussed previously in section 2.1, simulated temperature maps are generated by modeling the propagation of laser light and corresponding temperature increase using a FEM-based solver, which is also known as the forward problem. It is resolved by solving the diffusion equation (1-3) and Pennes bio-heat equation (4-5).

The performance of our algorithm is tested on a mice-sized 25 mm-diameter cylindrical phantom as shown in the first row of figure 9. The background absorption coefficient of the phantom is set to mimic small animal muscle tissue and is adjusted using black India ink and set to 0.01 mm$^{-1}$. The reduced scattering coefficient of the entire phantom was adjusted using intralipids and set to be equal to 0.86 mm$^{-1}$ [38]. To mimic the presence of orthotopic cancerous lesions (breast, ovarian, prostate, etc.) with different absorptions, we inserted inclusions having different sizes and higher absorption coefficients into the phantom. Here, no contrast in the scattering coefficient was used.
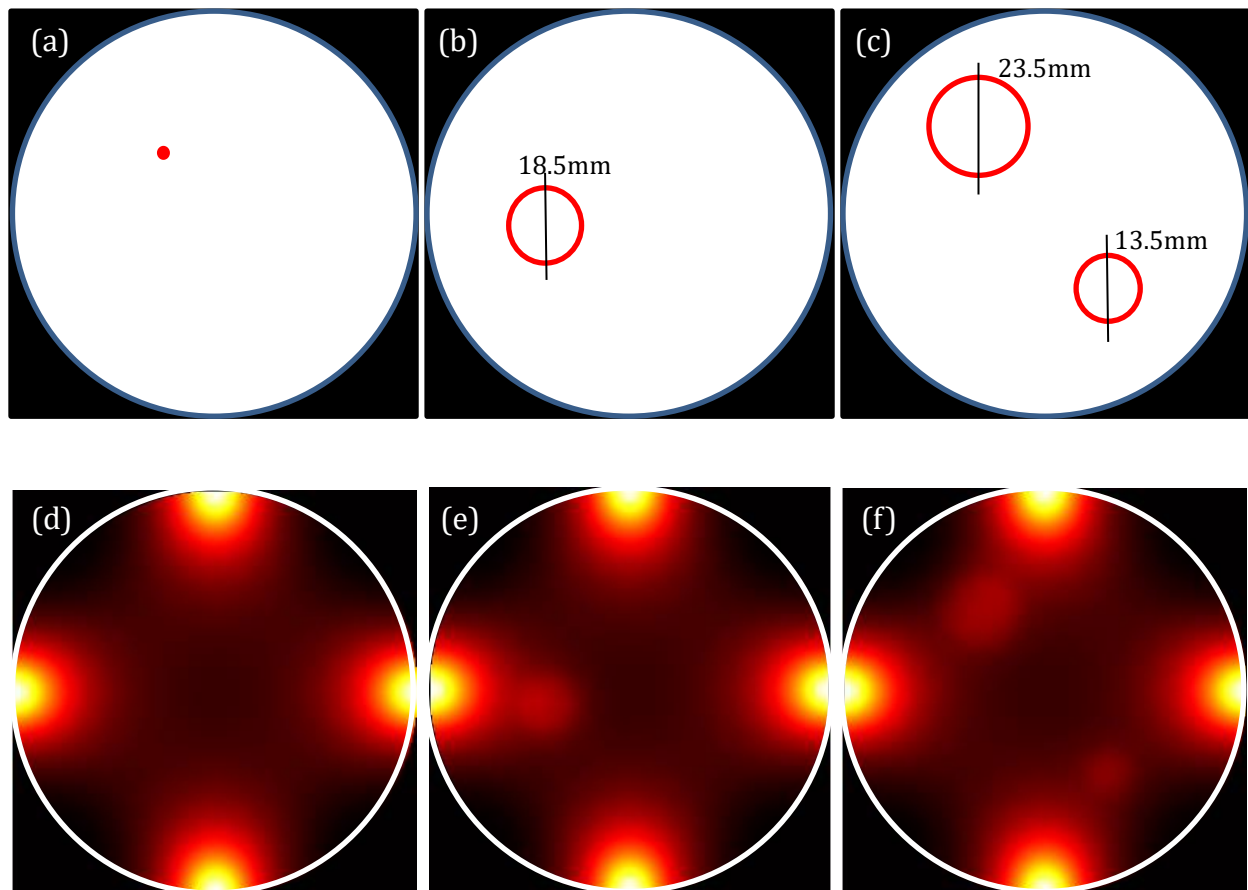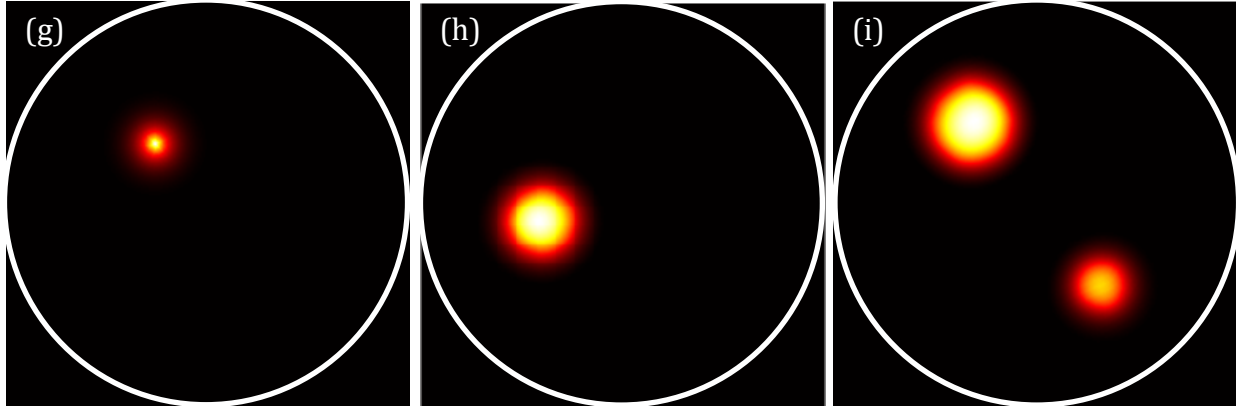
Figure 9: Representative phantoms used to generate the training data. a-c) Different sizes and location inclusions. All inclusions have an absorption coefficient twice higher as the background. d-f) The corresponding simulated temperature maps were obtained after 8 seconds of heating. g-i) The processed data after subtracting the homogenous temperature map obtained on a phantom without any inserted inclusion.

In the representative data presented in Fig. 9, the absorption coefficient is doubled at the mesh nodes that belong to the inclusions regions. Therefore, the heat signature at these locations would be greater than the surrounding medium. The first row in Fig. 9 depicts three kinds of phantoms that we utilized for the purposes of our data creation: a single node in the FEM, a single circular cluster of nodes, and finally, multiple clusters of nodes, with varying cluster radii. The second row of images depicts the simulation results of the temperature maps obtained after 8 seconds of heating. We can observe the high temperature increase straight below the four illumination sides, and that the temperature exponentially decays with depth, Fig. 9 d-f. However, we can see an increase in temperature within the inclusions despite their deep position. This is principally due to their higher absorption. The first step in the PMI image reconstruction algorithm is the estimation of the average background absorption [38, 40]. Once estimated, this absorption value is used to solve the forward problem of PMI and generate a temperature map called a *homogenous temperature map*. The last row of images depicts the processed heat maps after subtraction of the homogenous temperature map from the raw data shown in the second row. As you can see, before

any reconstruction process, we already notice the position of the inclusion. This is the main motivation of our research, since retrieving a priori information to help the image reconstruction algorithm seems trivial. In the following part of the thesis, we will describe and discuss different AI-based methodologies that we proposed to perform this task.

## 4.3 Method 1



**CNN model with one output neurons**
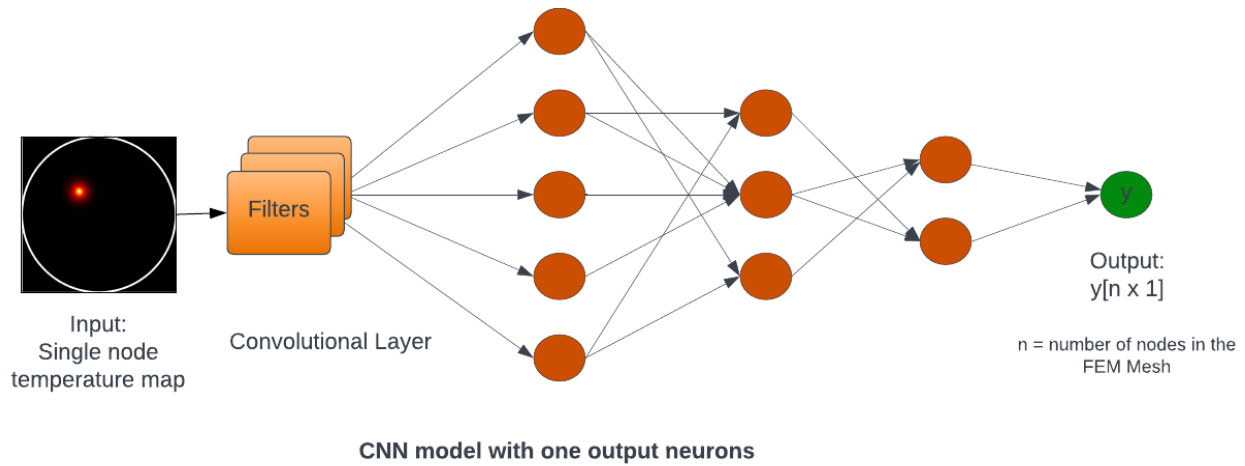
Figure 10: Visual representation of method 1

Initially, since our goal was to identify which nodes are responsible for the temperature blobs, we considered each node by itself and generate temperature maps by sequentially and individually increasing the absorption at each node. Since neural networks require huge amounts of data to train, each node (class) would require several images to be able to train and classify it. To generate these multiple images of the same class, i.e. node, the absorption coefficient of the nodes was variated within the range of biotissue values and temperature maps were generated for each value. In method 1, we used a simple Convolutional Neural Network to predict the nodes responsible for the heat blob. Let's call these nodes the *hot nodes*. This model was trained to predict only a single

node and showed a high performance in performing this task. The predicted node would show a high probability value within the output vector $y_k$.

However, when we tested this model to predict a cluster of nodes, that is more representative of a real tumorous region, it partially failed. Technically, the model continued to predict only one node with a higher probability. Nevertheless, we observed that the rest of the cluster hot nodes were also detected by their probability values were very weak, but still above the background node ones. Retrieving the whole cluster of hot nodes would require manual efforts, which motivated us to develop more autonomous methodologies. Hence, we decided to train the model using temperature maps containing multiple inclusions or clusters of hot nodes.

## 4.4 Method 2
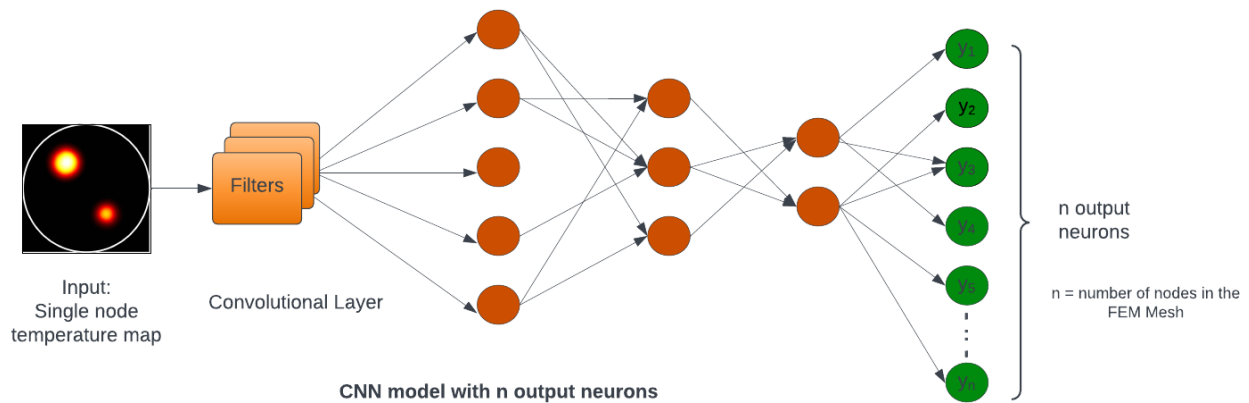


Figure 11: Visual representation of method 2

The major difference between method 1 and this one is that method 2 uses N neurons at its output layer. This allows it to detect each node directly through the activation of its corresponding neuron. Here, the network is trained to predict for each of the N mesh nodes individually. This was done by keeping all the layers the same as the previous convolutional neural network, but splitting the final layer into N output neurons. Now, instead of having a single [Nx1] vector of labels with N

elements to be trained for, we would directly have N output labels corresponding to each node. This network is modeled both as a linear (regression) model and a nonlinear model with sigmoidal activation.

Unlike in method 1, the convolutional neural network was trained with images containing multiple inclusions composed of a cluster of hot nodes. The training data is composed of pairs of data that contain a) the temperature image showing bright blobs, and b) the indices of the hot nodes. These node indices are also referred to as the ground truth. This ground truth vector would typically be a binary vector of length [Nx1] with ones assigned to the hot nodes and zeros elsewhere. Once trained and tested on several phantoms, this method showed poor performance with a maximum accuracy of approximately 22%.

In order to improve its performance, an alternative approach for the creation of the ground truth in the training pairs was adopted. Instead of using a binary vector, the values assigned to the hot nodes are normalized by the total number of hot nodes in the image. This approach drastically improved the accuracy of the method to reach a maximum accuracy of ~ 40%. The major drawback of the method is that, as the inclusion size increases, the number of hot nodes becomes important and directly results in a ground truth vector with weak values, which are comparable to the zero contribution of the background nodes.

## 4.5 Method 3 - Region Prediction and Precision Improvement

Considering the limited performance of both methods 1 and 2, the methodology finally adopted for our task was a two-step Region of Interest (ROI) localization or region prediction and subsequent precision improvement approach.

## 4.5.1 Method 3a – Region Prediction

Our new algorithm is based on a supervised Machine Learning approach. As for the data used for method 2, the training data used here is composed of a) the 256 x 256 pixels$^2$ temperature image showing bright blobs, and b) the indices of the hot nodes.
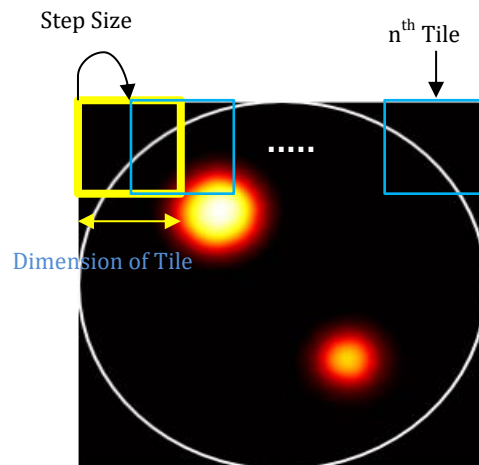


Figure 12: Visual representation of the division of sub-images using n x n tiles$^2$. The first tile is shown in yellow. The second tile is the adjacent one with an overlap of half the tile size.

The temperature maps were divided into overlapping sub-images (tiles). Each of the tiles overlaps with the adjacent tile with exactly half its size as shown in Fig. 12. Considering the size of the temperature maps, the sizes of sub-images are 64x64 pixels$^2$ when maps are divided into 7x7 tiles$^2$, 32x32 pixels$^2$ for 15x15 tiles$^2$ and 16x16 pixels$^2$ for 31x31 tiles$^2$. The mesh being used for demonstration purposes of our methodology contains 852 nodes.

| 7x7 Tiles$^2$ | 15x15 Tiles$^2$ | 64x64 Tiles$^2$ |
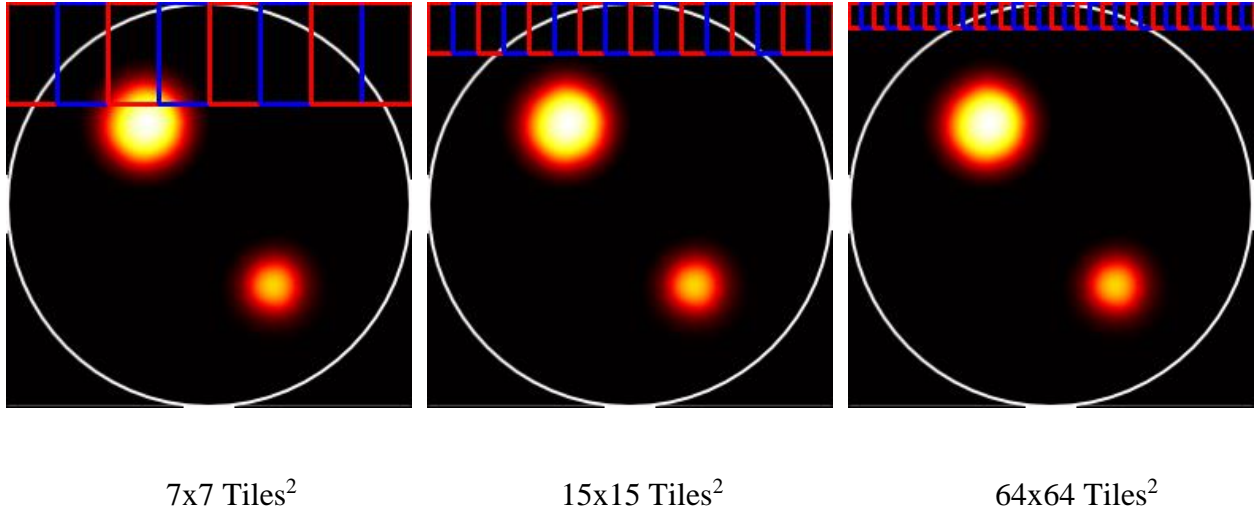
Figure 13: Visual representation of the division of sub-images for varying tiles size. The figure is only a representation showing the first row of tiles.

Secondly, each of the sub-images is assigned a binary label: '1' if the region contained the inclusion, '0' if not. The assignment of these values is decided by the spatial localization of the hot nodes within our overlapping tiles. Henceforth for this network, a sub-image and its corresponding binary label pair shall be referred to as *training pair*. Considering the nature of the data where most of the image corresponds to the background, the number of tiles labeled as 1 is very few compared to the ones labeled 0. Thus, further preprocessing is done on this data to simply eliminate most of the 0 data and ensure that the proportion of the two classes in the data is equal. This is to ensure that there are no inherent biases in the data that might be accidentally learned by our ML classifier.

Thirdly, these training pairs are fed to the ML Classifier model composed of six layers, Fig. 14. The output layer contains a single neuron or a single output. The activation function associated with this layer is chosen to be the sigmoidal nonlinearity. This is done to constrain the output of the neural network to values between 0 and 1. The neural network learns by computing the error between ground truth labels and the predicted output labels. This error is then backpropagated

throughout the network to adjust the learning parameters of the model using gradient-based optimization methods. The optimization method used for our methodology was the *Adam Optimizer*. The training process of the network is stopped when a set accuracy above 90% is reached and the loss converges. The training process typically contains the evaluation of the model's performance over a set of training pairs extracted from the training pairs inputted into the model. This data is called the validation data. Accuracy is computed over the entire set of validation data. The network has been trained for 5 epochs in total. Epochs generally refer to the number of times our model is trained iteratively to fit over the set of given training pairs.
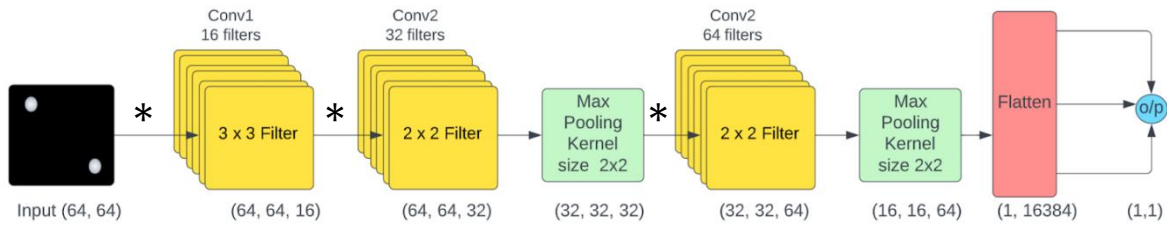


Figure 14: Structure of the ML Classifier model used in method 3.

Finally, once the classification process is achieved, the tiles are classified into two classes: 1) positive labeled as 1, and 2) negative labeled as 0. For each of the positive regions, we perform an intersection over union on the sets of nodes belonging to each of these positive tiles. The final set of nodes obtained is said to be the predicted nodes that will be compared to the ground truth hot nodes to calculate the accuracy of this methodology. Although highly performant, this method still required additional improvement to reach significant accuracies.

## 4.5.2 Method 3b - Precision Improvement using Regression
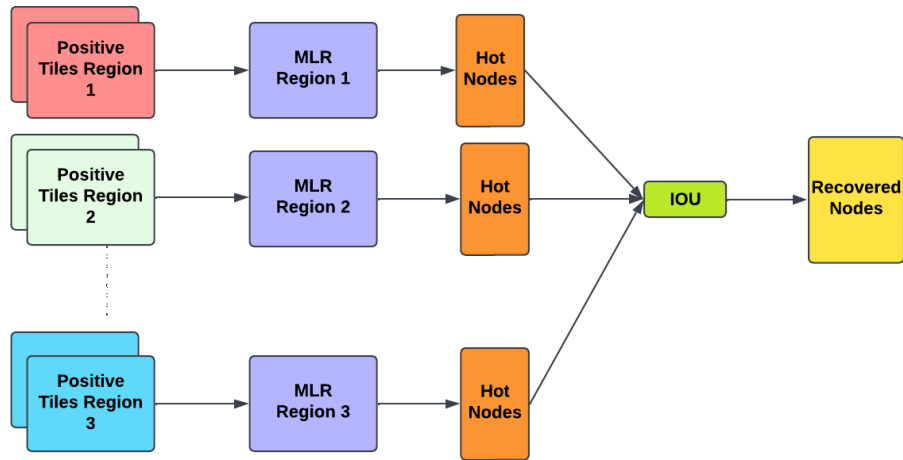


Figure 15: Precision improvement pipeline for prediction of nodes

Method 3a yielded low hot node prediction accuracies. These low accuracies were largely due to falsely positive predicted nodes and a small percentage of false negative predicted nodes after the Intersection over Union method. Up to here, if the tile was classified as positive, all the nodes belonging to it were assumed to be predicted as hot nodes. To improve method 3a, we tried a new weighted concept that allows us to better predict the hot nodes. And several such approaches were tried to improve the reconstruction accuracy, but we quickly acknowledged that region-based information would not be entirely sufficient in the accurate prediction of the entire set of hot nodes. Indeed, pixel-level information of these tile regions would be required to produce much higher accuracy predictions.

Several approaches were tried to improve the reconstruction accuracy but it was quickly acknowledged that region information would not be entirely sufficient in the prediction of the contributing nodes in the mesh. The pixel-level information of these regions would be required to produce the necessary results.

In Method 2, the attempt to predict the contributions of each of the nodes from the temperature maps drove us into a well-known problem of 'data sparsity'. Each of the images when mapped to the label of the nodes in the mesh, the number of zeros or 'off nodes' far outweighed the number of 'hot nodes'. Therefore, were any ML model to fit on such label vectors would overfit to the zeros of output. Similarly, there was only a small percentage of useful information or non–zero pixels in the temperature maps for the ML model to train for.

To circumvent the problem of data sparsity and subsequent overfitting of our ML models, we decided to use an approach that samples only the useful information from our complete temperature maps. Useful information is constituted by a significant amount of non-zero pixels constituting the inclusion and zero pixels of the background.

Firstly the full-sized image was processed by our CNN to retain the positive tiles for each image. A 7x7 division scheme was picked for this task. This division size was chosen to retain only the useful information from the full-sized image in the positive tile. From our data pool of 3927 full-sized images, we employed the CNN model to aggregate positive tile examples for each of the 49 regions and created 49 different image training data. We mapped each tile to the subset of hot nodes lying in the region. A training pair for each region constituted the positive tile and the set of hot nodes in the tile. A multi-linear regression (MLR) model was fit to these training pairs as shown in Fig. 15.

A full-sized test image was passed through our final pipeline, obtaining the positive tiles from CNN and subsequent contributory nodes for each of the tiles. An intersection over union of contributory nodes as predicted by all tiles was performed and accuracy as an intersection of

predicted nodes with the ground truth was calculated. This method demonstrated promising results

for our test cases, with mean node recovery accuracy of 95.35%.

# Chapter 5: Result and Discussion

Considering the poor results obtained using methods 1 and 2 and for the sake of the thesis's limited number of pages, we preferred to omit the presentation of those results. The quantitative accuracy of these methods has been provided during the presentation of the method in sections 4.1 and 4.2.

## 5.1 Prediction using Method 3a

A set of testing data is generated in order to test our ML model. Results obtained on a representative phantom bearing two inclusions of different sizes are presented below, Fig. 16, 17, and 18. In these figures, the red circles show the predicted nodes by the AI and the black asterisks show the ground truth hot nodes. Figures 16, 17, and 18 respectively show the results obtained by when our ML is trained using 7x7, 15x15, and 31x31 tiles[2].
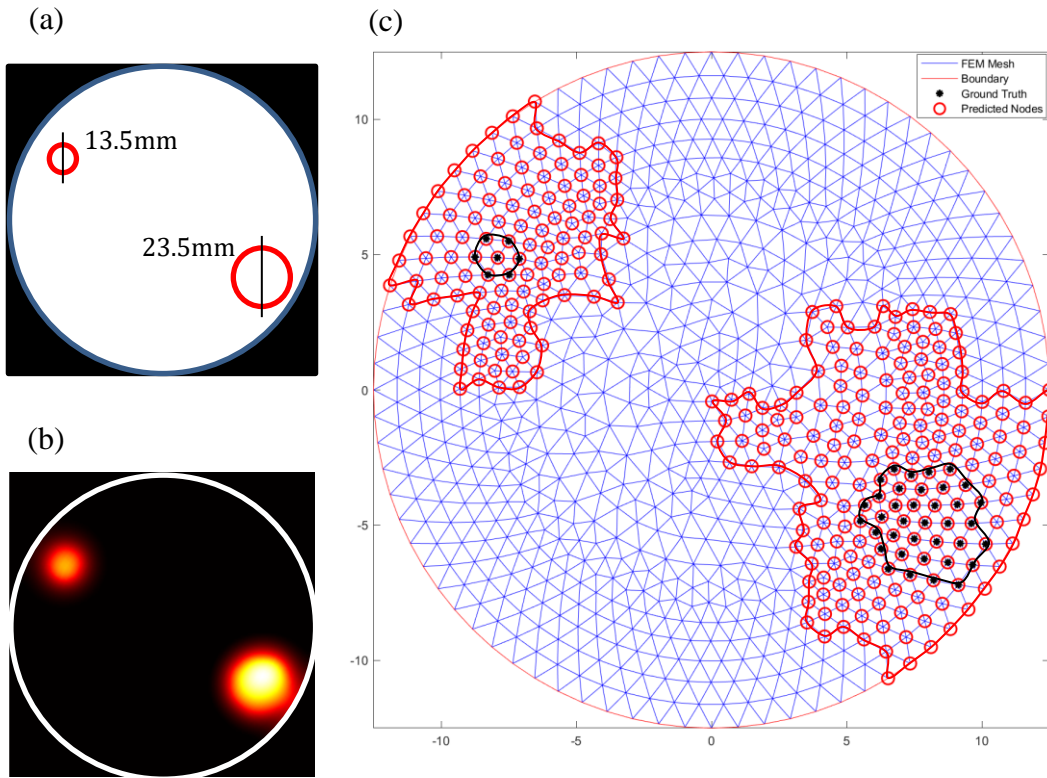
Figure 16: a) Schematic of the phantom. b) temperature map. c) Results obtained using method 3a when trained with 7x7 tiles[2].
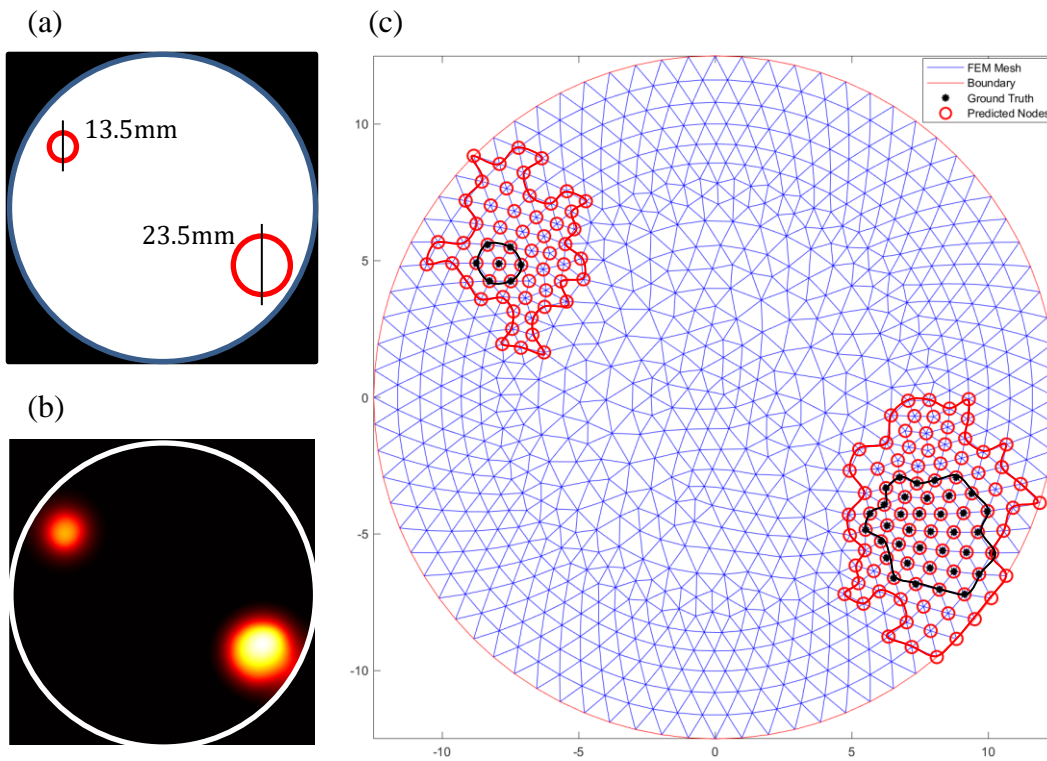
Figure 17: a) Schematic of the phantom. b) temperature map. c) Results obtained using method 3a when trained with 15x15 tiles[2].

(a)

(c)

(b)
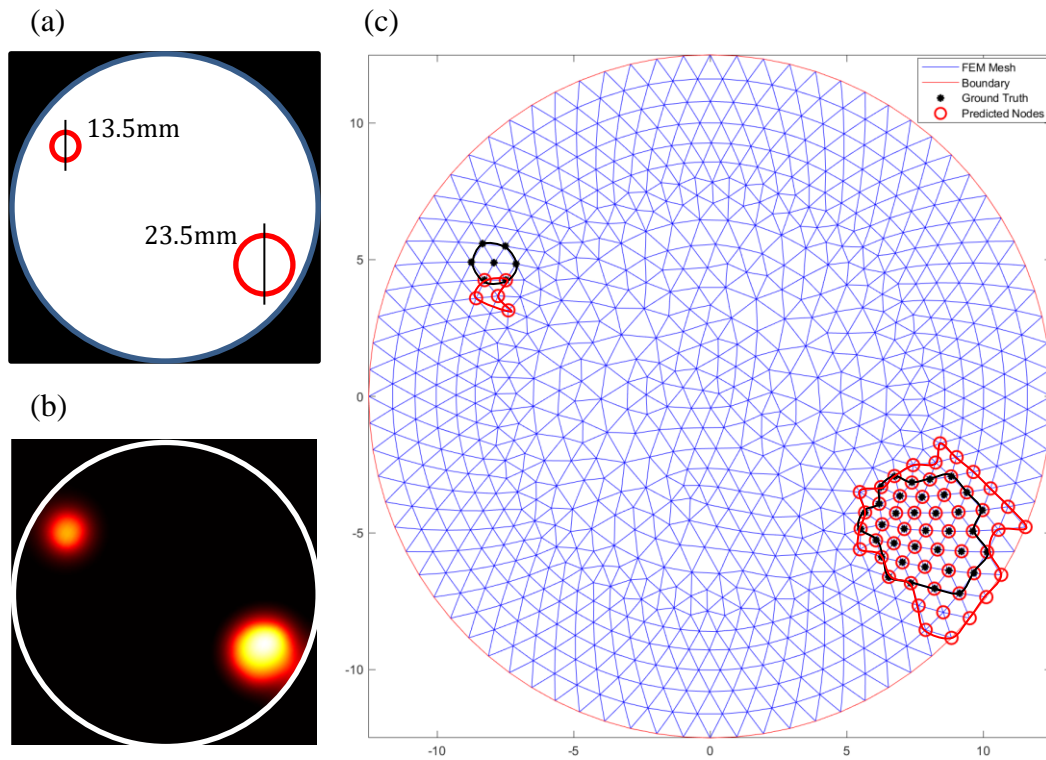
Figure 18: a) Schematic of the phantom. b) temperature map. c) Results obtained using method 3a when trained with 31x31 tiles[2].

In all the results obtained on the testing images above, we can observe that our algorithm is able to predict the actual hot nodes, but also predicts additional nodes around it. These additional nodes are falsely detected as positive nodes. We can observe a decrease in the number of false positives as we decrease the size of the tiles, which results in a more accurate prediction of the hot nodes. However, one can notice that the algorithm was not able to detect the totality of the hot nodes in the small inclusion and showed a shift of two triangular mesh elements. A summary of the performance of our method is presented in Table 1.

| Total number of used tiles | Accuracy obtained by the ML model (%) | Average percentage of nodes predicted on test data (%) |
|---|---|---|
| 7x7 = 49 | 97.14% | ≈ 19% |
| 15x15 = 225 | 95.25% | ≈ 42% |
| 31x31 = 961 | 94.36% | ≈ 53% |

Table 1: Accuracies obtained when our ML is trained using 7x7, 15x15, and 31x31 tiles[2]. The average percentage of nodes predicted is also provided.

## 5.2 Prediction using Method 3b

Method 3b is implemented to tackle the limitations faced by method 3a. The following sections discuss the performance of method 3b on various types of data.
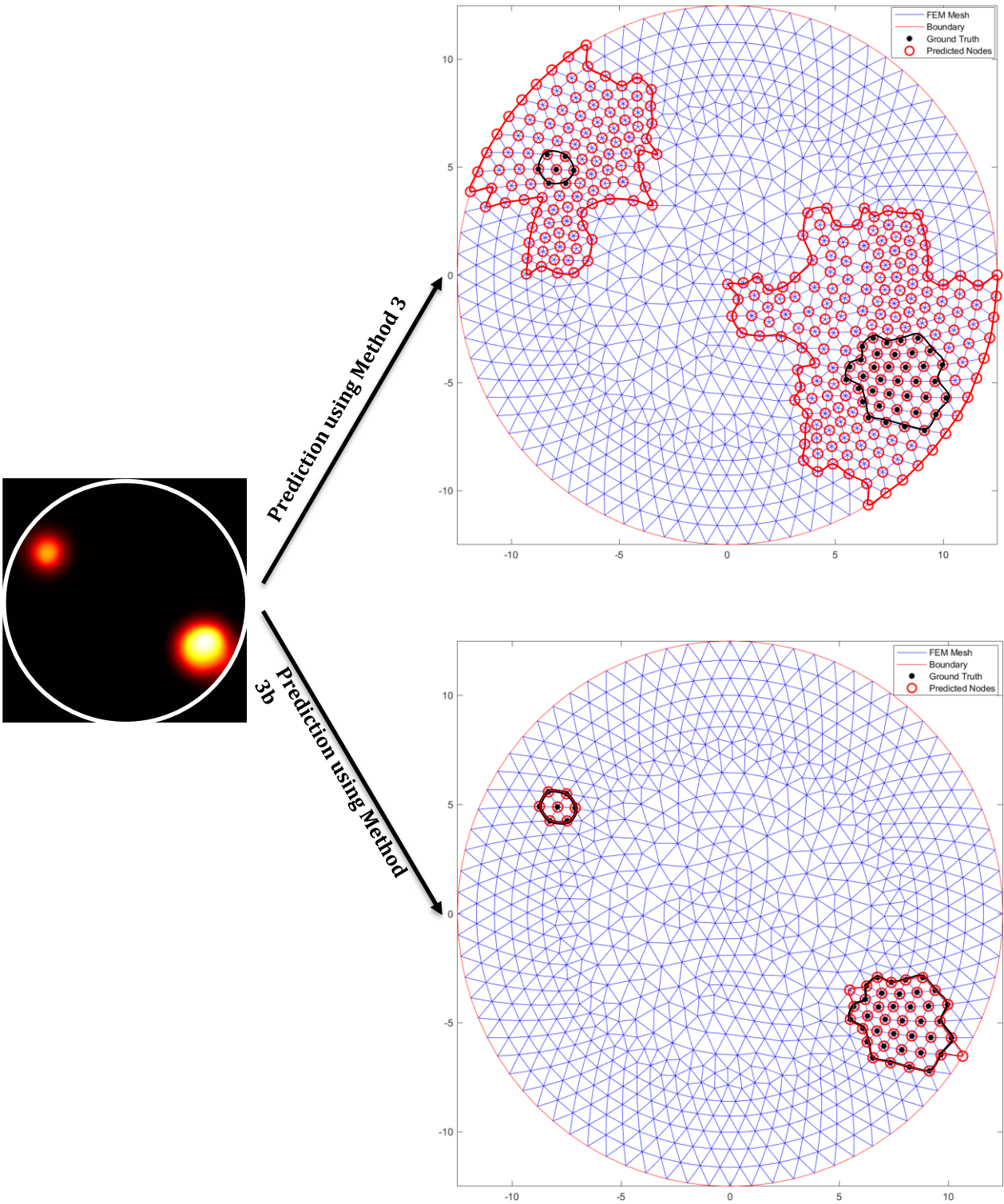
Figure 19: a) Temperature map. b) Result obtained using method 3a. c) Result obtained using

method 3b

Results will be presented in terms of quantitative metrics calculated as follows:

$$Percentage\ overlap\ with\ ground\ truth = \frac{Length\ of\ intersection\ array}{Length\ of\ ground\ truth\ array}$$

$$Predicted\ nodes\ array\ accuracy = \frac{Length\ of\ intersection\ array}{Length\ of\ total\ predicted\ array}$$

where the intersection array is composed of the nodes present in both the predicted and the ground truth hot nodes.

## 5.2.1 Results by varying the inclusion size
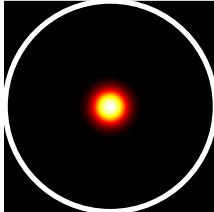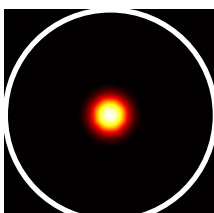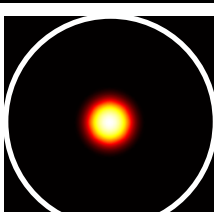
| Image | Diameter of Inclusion (in mm) | Percentage overlap with ground truth | Predicted nodes array accuracy |
|---|---|---|---|
|  | 16.5mm | 83.33% | 88.23% |
|  | 18.5mm | 85% | 94.44% |
|  | 23.5mm | 100% | 100% |

Table 2: Prediction on testing data using method 3b for phantoms bearing inclusions with varying diameters. The inclusions are positioned at the center of the phantom and have an absorption coefficient twice higher than the background.

## 5.2.2 Results by varying the number of inclusions in the image

This table shows the same accuracies for single and multiple inclusions which are far away from each other and nearby.
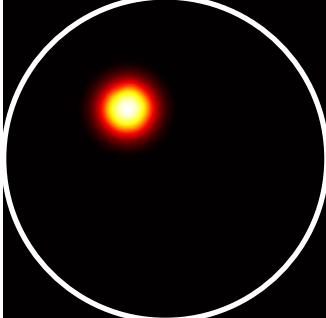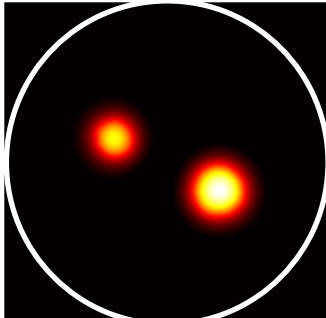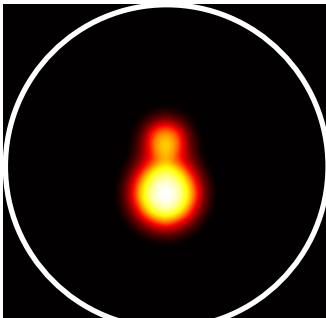
| Image | Diameter of Inclusion (in mm) | Percentage overlap with ground truth | Predicted nodes array accuracy |
|---|---|---|---|
|  | 18.5mm | 100% | 93.23% |
|  | Small Inclusion = 10mm<br><br>Larger Inclusion = 18.5mm | 100% | 95.23% |
|  | Small Inclusion = 11.5mm<br><br>Larger Inclusion = 25mm | 92.68% | 95% |

Table 3: Prediction on testing data using method 3b for phantoms bearing single and multiple inclusions. The inclusions have an absorption coefficient twice higher than the background.

# Chapter 6: Conclusion and Future Work

In this thesis, we examined the reconstruction of cancerous regions within a phantom using Image and Machine Learning computational methods. This experiment was performed for various sizes and orientations of cancerous clusters mainly concentrating on achieving high accuracies for multiple interacting inclusions in the medium. Results show that our method produces a reliable and robust recovery of the cancerous regions straight from the temperature maps. The obtained result will be directly used to build the penalty matrix that will be employed to constrain and guide the PMI image reconstruction algorithm.

All the methods developed within the framework of this thesis have been generated on phantoms bearing inclusions mimicking tumors. These inclusions have different sizes and locations. The optical absorption of these inclusions was doubled to model the higher concentration of the main chromophores within tumors. Our approach demonstrated high performance characterized by accuracy as high as 97.8%. The algorithm allows the prediction of the hot nodes in any MRT temperature map in 2.8 seconds using the servers of Google Colaboratory (16GB RAM being used for this task).

Prior to our research, a priori functional information from the temperature maps was never utilized for guiding the reconstruction process as described by Eq. 7. Our research introduces the first-ever use of a priori information for reconstruction as given by Eq. 8. Our method provides a significant advantage by drastically accelerating the convergence of the PMI algorithm. Moreover, this is the first ever AI-based methodology being implemented in the Centre for Functional Onco-Imaging (CFOI). At the end of this research, we developed the necessary tools using Convolutional Neural Networks and Regression-based methods for driving the reconstruction process from MRT

temperature maps. Our work fosters research in the interdisciplinary field of AI and Biomedical Imaging, demonstrating the promising opportunity for graduate students and researchers to mature their ideas into viable working solutions.

# References

[1] J.C. Hebden, S.R. Arridge, D.T. Delpy, Optical imaging in medicine: I. Experimental techniques, Phys Med Biol 42(5) (1997) 825-40.

[2] S.R. Arridge, J.C. Hebden, Optical imaging in medicine: II. Modelling and reconstruction, Phys Med Biol 42(5) (1997) 841-53.

[3] A. Gibson, J. Hebden, S.R. Arridge, Recent advances in diffuse optical imaging, Physics in medicine and biology 50(4) (2005) R1.

[4] A. Gibson, H. Dehghani, Diffuse optical imaging, Philos Trans A Math Phys Eng Sci 367(1900) (2009) 3055-72.

[5] H. Dehghani, S. Srinivasan, B.W. Pogue, A. Gibson, Numerical modelling and image reconstruction in diffuse optical tomography, Philos Trans A Math Phys Eng Sci 367(1900) (2009) 3073-93.

[6] A.T. Eggebrecht, S.L. Ferradal, A. Robichaux-Viehoever, M.S. Hassanpour, H. Dehghani, A.Z. Snyder, T. Hershey, J.P. Culver, Mapping distributed brain function and networks with diffuse optical tomography, Nat Photonics 8(6) (2014) 448-454.

[7] F. Nouizi, GilbertoDiaz-Ayil, F. XavierBlé, BenoitDubois, WilfriedUhring, P. Poulet, Time-gated near-infrared spectroscopic imaging of brain activation: a simulation proof of concept, SPIE BiOS, SPIE, San Francisco, 2011, pp. 78960L-78960L.

[8] F. Nouizi, M. Torregrossa, O. Geneveaux, R. Chabrier, P. Poulet, 3D modeling of noncontact fiber-based approach for time-resolved diffuse optical tomography, SPIE BiOS, International Society for Optics and Photonics, 2011, pp. 78961Z-78961Z-8.

[9] F. Nouizi, M. Torregrossa, R. Chabrier, P. Poulet, Improvement of absorption and scattering discrimination by selection of sensitive points on temporal profile in diffuse optical tomography, Opt Express 19(13) (2011) 12843-54.

[10] F. Nouizi, Preclinical, fluorescence and diffuse optical tomography: non-contact instrumentation, modeling and time-resolved 3D reconstruction, France, 2011, p. 174.

[11] F. Nouizi, G. Diaz-Ayil, F.-X. Blé, B. Dubois, W. Uhring, P. Poulet, Time-gated near-infrared spectroscopic imaging of brain activation: a simulation proof of concept, in: SPIE (Ed.) SPIE BIOS, International Society for Optics and Photonics, San Francisco, 2011, pp. 78960L-78960L-8.

[12] F. Gao, M. Jing, J. Li, F. Nouizi, P. Poulet, L. Zhang, H. Zhao, A fiber-based, non-contact scheme for time-domain diffuse fluorescence tomography: methodology and simulative validation, SPIE BiOS, International Society for Optics and Photonics, 2010, pp. 75570O-75570O-9.

[13] F. Nouizi, R. Chabrier, M. Torregrossa, P. Poulet, 3D modeling for solving forward model of no-contact Fluorescence Diffuse Optical Tomography method, European Conferences on Biomedical Optics, International Society for Optics and Photonics, Munich, Germany, 2009, pp. 73690C-73690C-10.

[14] Y. Lin, D. Thayer, O. Nalcioglu, G. Gulsen, Tumor characterization in small animals using magnetic resonance-guided dynamic contrast enhanced diffuse optical tomography, J Biomed Opt 16(10) (2011) 106015.

[15] M.B.U. David Thayer, Yuting Lin, Kevin Yan, Orhan Nalcioglu, Gultekin Gulsen, Dual-Contrast Dynamic MRI-DOT for Small Animal Imaging, Technology in cancer research and treatment 9(1) (2010) 10.

[16] Y. Lin, W.C. Barber, J.S. Iwanczyk, N.E. Hartsough, W. Roeck, O. Nalcioglu, G. Gulsen, Quantitative fluorescence tomography using a combined tri-modality FT/DOT/XCT system, Optics Express 18(8) (2010) 7835–7850.

[17] A. Farina, M. Betcke, L. Di Sieno, A. Bassi, N. Ducros, A. Pifferi, G. Valentini, S. Arridge, C. D'Andrea, Multiple-view diffuse optical tomography system based on time-domain compressive measurements, Optics letters 42(14) (2017) 2822-2825.

[18] M. Alayed, M.A. Naser, I. Aden-Ali, M.J. Deen, Time-resolved diffuse optical tomography system using an accelerated inverse problem solver, Optics express 26(2) (2018) 963-979.

[19] H. Erkol, F. Nouizi, A. Luk, B. Unlu, G. Gulsen, An Analytical Approach for Temperature Distribution in Tissue, Optical Tomography and Spectroscopy, Optical Society of America, 2016, p. JW3A. 12.

[20] H. Erkol, F. Nouizi, M.B. Unlu, G. Gulsen, An extended analytical approach for diffuse optical imaging, Physics in medicine and biology 60(13) (2015) 5103.

[21] M.L. Altoe, A. Marone, H.K. Kim, K. Kalinsky, D.L. Hershman, A.H. Hielscher, R.S. Ha, Diffuse optical tomography of the breast: a potential modifiable biomarker of breast cancer risk with neoadjuvant chemotherapy, Biomedical optics express 10(8) (2019) 4305-4315.

[22] H. Vavadi, A. Mostafa, F. Zhou, K.S. Uddin, M. Althobaiti, C. Xu, R. Bansal, F. Ademuyiwa, S. Poplack, Q. Zhu, Compact ultrasound-guided diffuse optical tomography system for breast cancer imaging, Journal of biomedical optics 24(2) (2018) 021203.

[23] J. Ruiz, F. Nouizi, J. Cho, J. Zheng, Y. Li, J.-H. Chen, M.-Y. Su, G. Gulsen, Breast density quantification using structured-light-based diffuse optical tomography simulations, Applied optics 56(25) (2017) 7146-7157.

[24] J. Kwong, F. Nouizi, J. Cho, J. Zheng, Y. Li, J. Chen, M. Su, G. Gulsen, Diffuse optical imaging of the breast using structured-light, SPIE BiOS, International Society for Optics and Photonics, 2015, pp. 93190K-93190K-5.

[25] D. Lighter, J. Hughes, I. Styles, A. Filer, H. Dehghani, Multispectral, non-contact diffuse optical tomography of healthy human finger joints, Biomedical optics express 9(4) (2018) 1445-1460.

[26] M.D. Wheelock, J.P. Culver, A.T. Eggebrecht, High-density diffuse optical tomography for imaging human brain function, Review of Scientific Instruments 90(5) (2019) 051101.

[27] B.J. Tromberg, Z. Zhang, A. Leproux, T.D. O'Sullivan, A.E. Cerussi, P.M. Carpenter, R.S. Mehta, D. Roblyer, W. Yang, K.D. Paulsen, Predicting responses to neoadjuvant chemotherapy in breast cancer: ACRIN 6691 trial of diffuse optical spectroscopic imaging, Cancer research 76(20) (2016) 5933-5944.

[28] A. Leproux, A. Durkin, M. Compton, A.E. Cerussi, E. Gratton, B.J. Tromberg, Assessing tumor contrast in radiographically dense breast tissue using Diffuse Optical Spectroscopic Imaging (DOSI), Breast Cancer Res 15(5) (2013) R89.

[29] T.D. O'Sullivan, A. Leproux, J.H. Chen, S. Bahri, A. Matlock, D. Roblyer, C.E. McLaren, W.P. Chen, A.E. Cerussi, M.Y. Su, B.J. Tromberg, Optical imaging correlates with magnetic resonance

imaging breast density and reveals composition changes during neoadjuvant chemotherapy, Breast Cancer Res 15(1) (2013) R14.

[30] S.R. Arridge, W.R.B. Lionheart, Non-uniqueness in diffusion-based optical tomography, Opt. Lett. 23(11) (1998) 882.

[31] S. Arridge, Optical tomography in medical imaging, Inverse Problems 15(2) (1999) R41-R93.

[32] L.V. Wang, Prospects of photoacoustic tomography, Medical physics 35(12) (2008) 5758-5767.

[33] P. Burgholzer, J. Bauer-Marschallinger, B. Reitinger, T. Berer, Resolution limits in photoacoustic imaging caused by acoustic attenuation, Journal of Imaging 5(1) (2019) 13.

[34] S.S. Alshahrani, Y. Yan, N. Alijabbari, A. Pattyn, I. Avrutsky, E. Malyarenko, J. Poudel, M. Anastasio, M. Mehrmohammadi, All-reflective ring illumination system for photoacoustic tomography, Journal of biomedical optics 24(4) (2019) 046004.

[35] M. Nishiyama, T. Namita, K. Kondo, M. Yamakawa, T. Shiina, Ring-array photoacoustic tomography for imaging human finger vasculature, Journal of biomedical optics 24(9) (2019) 096005.

[36] D.A. Thayer, Y. Lin, A. Luk, G. Gulsen, Laser-induced photo-thermal magnetic imaging, Appl Phys Lett 101(8) (2012) 83703.

[37] Y. Lin, D. Thayer, A. Luk, G. Gulsen, Laser-Induced Photo-thermal Magnetic Imaging, Applied Physics Letters in press (2012).

[38] F. Nouizi, A. Luk, D. Thayer, Y. Lin, S. Ha, G. Gulsen, Experimental validation of a high-resolution diffuse optical imaging modality: photomagnetic imaging, J Biomed Opt 21(1) (2016) 16009.

[39] F. Nouizi, M. Algarawi, H. Erkol, A. Luk, G. Gulsen, Multiwavelength photo-magnetic imaging algorithm improved for direct chromophore concentration recovery using spectral constraints, Applied Optics 60(35) (2021) 10855-10861.

[40] M. Algarawi, H. Erkol, A. Luk, S. Ha, M. Burcin Unlu, G. Gulsen, F. Nouizi, Multi-Wavelength Photo-Magnetic Imaging System for Photothermal Therapy Guidance, Lasers in Surgery and Medicine (2020).

[41] M. Algarawi, A. Luk, H. Erkol, M. Almudhry, B.M. Unlu, G. Gulsen, F. Nouizi, Reconstruction chromophore concentration directly by Photo-Magnetic Imaging: simulation study, Optical Tomography and Spectroscopy, Optical Society of America, 2020, p. JTu3A. 15.

[42] M. Algarawi, H. Erkol, A. Luk, S. Ha, M.B. Ünlü, G. Gulsen, F. Nouizi, Resolving tissue chromophore concentration at MRI resolution using multi-wavelength photo-magnetic imaging, Biomedical Optics Express 11(8) (2020) 4244-4254.

[43] M. Algarawi, F. Nouizi, A. Luk, M. Mehrabi, H. Erkol, M.B. Ünlü, G. Gulsen, S. Ha, High-resolution chromophore concentration recovery using multi-wavelength photo-magnetic imaging, Multimodal Biomedical Imaging XIV, International Society for Optics and Photonics, 2019, p. 108710F.

[44] F. Nouizi, H. Erkol, A. Luk, M. Algarawi, M. Mehrabi, G. Gulsen, Multi-wavelengths Photo Magnetic Imaging, Optical Tomography and Spectroscopy, Optical Society of America, 2018, p. JW3A. 45.

[45] A. Luk, F. Nouizi, H. Erkol, M.B. Unlu, G. Gulsen, Ex vivo validation of photo-magnetic imaging, Optics letters 42(20) (2017) 4171-4174.

[46] A.T. Luk, F. Nouizi, M. Marks, T. Kart, G. Gulsen, Monitoring gold nanoparticle distribution with high resolution using photo-magnetic imaging, Optical Interactions with Tissue and Cells XXVII, International Society for Optics and Photonics, 2016, p. 97060M.

[47] F. Nouizi, H. Erkol, A. Luk, M. Marks, M.B. Unlu, G. Gulsen, An accelerated photo-magnetic imaging reconstruction algorithm based on an analytical forward solution and a fast Jacobian assembly method, Phys Med Biol 61(20) (2016) 7448-7465.

[48] F. Nouizi, H. Erkol, A. Luk, Y. Lin, G. Gulsen, Analytical Photo Magnetic Imaging, Optical Tomography and Spectroscopy, Optical Society of America, 2016, p. OW4D. 7.

[49] F. Nouizi, H. Erkol, A. Luk, M.B. Unlu, G. Gulsen, Real-time photo-magnetic imaging, Biomedical Optics Express 7(10) (2016) 3899-3904.

[50] H. Erkol, F. Nouizi, A. Luk, M.B. Unlu, G. Gulsen, Comprehensive analytical model for CW laser induced heat in turbid media, Optics Express 23(24) (2015) 31069-31084.

[51] A.T. Luk, S. Ha, F. Nouizi, D. Thayer, Y. Lin, G. Gulsen, A true multi-modality approach for high resolution optical imaging: photo-magnetic imaging, SPIE BiOS, International Society for Optics and Photonics, 2014, pp. 89370G-89370G-7.

[52] A.T. Luk, D. Thayer, Y. Lin, F. Nouizi, H. Gao, G. Gulsen, A novel high-resolution optical imaging modality: photo-magnetic imaging, SPIE BiOS, International Society for Optics and Photonics, 2013, pp. 857404-857404-6.

[53] F. Nouizi, T.C. Kwong, J. Cho, Y. Lin, U. Sampathkumaran, G. Gulsen, Implementation of a new scanning method for high-resolution fluorescence tomography using thermo-sensitive fluorescent agents, Opt Lett 40(21) (2015) 4991-4.

[54] D. Nikkhah, F. Nouizi, R. Hurtado, P. Tabatabaei, G. Gulsen, Temperature Modulated Fluorescence Tomography Feasibility Using an Intensified CCD Camera, Optics and the Brain, Optica Publishing Group, 2022, p. JM3A. 9.

[55] F. Nouizi, H. Erkol, D. Nikkhah, T.C. Kwong, G. Gulsen, Development of a preclinical CCD-based temperature modulated fluorescence tomography platform, Biomedical Optics Express 13(11) (2022) 5740-5752.

[56] T.C. Kwong, F. Nouizi, Y. Lin, J. Cho, Y. Zhu, U. Sampathkumaran, G. Gulsen, Experimental evaluation of the resolution and quantitative accuracy of temperature-modulated fluorescence tomography, Applied optics 56(3) (2017) 521-529.

[57] T.C. Kwong, F. Nouizi, J. Cho, Y. Lin, U. Sampathkumaran, G. Gulsen, Feasibility study of high spatial resolution multimodality fluorescence tomography in ex vivo biological tissue, Applied optics 56(28) (2017) 7886-7891.

[58] Y. Lin, F. Nouizi, T.C. Kwong, G. Gulsen, Simulation-based evaluation of the resolution and quantitative accuracy of temperature-modulated fluorescence tomography, Appl Opt 54(25) (2015) 7612-21.

[59] T.C. Kwong, F. Nouizi, Y. Lin, Y. Sampathkumaran, A. Shaaz, G. Gulsen, Temperature-modulated fluorescence tomography: modulating tissue temperature using HIFU for high-resolution in vivo fluorescence tomography, SPIE BiOS, 2013, pp. 857405-857405-8

[60] B.P. P. Yalavarthy, H. Dehghani, C. Carpenter, S. Jiang, and K. Paulsen, Structural information within regularization matrices improves near infrared diffuse optical tomography, Opt. Express 15 (2007) 8043-8058.

[61] H. Dehghani, M.E. Eames, P.K. Yalavarthy, S.C. Davis, S. Srinivasan, C.M. Carpenter, B.W. Pogue, K.D. Paulsen, Near infrared optical tomography using NIRFAST: Algorithm for numerical model and image reconstruction, Communications in numerical methods in engineering 25(6) (2009) 711-732.

[62] Y. Lin, H. Gao, D. Thayer, A.L. Luk, G. Gulsen, Photo-magnetic imaging: resolving optical contrast at MRI resolution, Phys Med Biol 58(11) (2013) 3551-62.

[63] F. Nouizi, J. Brooks, D.M. Zuro, S.K. Hui, G. Gulsen, Implementation of a combined theranostic x-ray irradiator/fluorescence imaging system for automatic assessment of tumor vascular response to radiation therapy, Multiscale Imaging and Spectroscopy III, SPIE, 2022, pp. 15-19.

[64] F. Nouizi, J. Brooks, D.M. Zuro, S.K. Hui, G. Gulsen, Theranostic Fluorescence Tomography-Guided Small Animal X-ray Irradiator Platform: System Development and Validation, Optical Tomography and Spectroscopy, Optica Publishing Group, 2022, p. OTu2D. 7.

[65] F. Nouizi, T.C. Kwong, J. Ruiz, J. Cho, Y.-W. Chan, K. Ikemura, H. Erkol, U. Sampathkumaran, G. Gulsen, A thermo-sensitive fluorescent agent based method for excitation light leakage rejection for fluorescence molecular tomography, Physics in medicine and biology (2018).

[66] T.C. Kwong, F. Nouizi, U. Sampathkumaran, Y. Zhu, M.M. Alam, G. Gulsen, Activatable thermo-sensitive ICG encapsulated pluronic nanocapsules for temperature sensitive fluorescence tomography, SPIE BiOS, International Society for Optics and Photonics, 2015, pp. 93390C-93390C-6.

[67] F. Nouizi, T.C. Kwong, J. Kwong, J. Cho, Y. Chan, U. Sampathkumaran, Y. Zhu, M.M. Alam, G. Gulsen, Excitation light leakage suppression using temperature sensitive fluorescent agents, SPIE BiOS, International Society for Optics and Photonics, 2015, pp. 93190Y-93190Y-5.

[68] J. Kwong, F. Nouizi, Y. Li, J. Chen, M. Su, G. Gulsen, Simulation of optical breast density measurements using structured light illumination, SPIE BiOS, International Society for Optics and Photonics, 2014, pp. 893717-893717-8.

[69] S.R. Arridge, M. Schweiger, Image reconstruction in optical tomography, Philos Trans R Soc Lond B Biol Sci 352(1354) (1997) 717-26.

[70] E.H. Wissler, Pennes' 1948 paper revisited, J Appl Physiol (1985) 85(1) (1998) 35-41.

[71] H. Erkol, F. Nouizi, A.T. Luk, M.B. Unlu, G. Gulsen, A new analytical approach for heat generation in tissue due to laser excitation (Conference Presentation), Optical Interactions with Tissue and Cells XXVII, International Society for Optics and Photonics, 2016, p. 97060L.

[72] D.W. Marquardt, An algorithm for least-squares estimation of nonlinear parameters, Journal of the society for Industrial and Applied Mathematics 11(2) (1963) 431-441.

[73] B. Brooksby, B.W. Pogue, S. Jiang, H. Dehghani, S. Srinivasan, C. Kogel, T.D. Tosteson, J. Weaver, S.P. Poplack, K.D. Paulsen, Imaging breast adipose and fibroglandular tissue molecular signatures by using hybrid MRI-guided near-infrared spectral tomography, Proc Natl Acad Sci U S A 103(23) (2006) 8828-33.

[74] F. El-Ghussein, M.A. Mastanduno, S. Jiang, B.W. Pogue, K.D. Paulsen, Hybrid photomultiplier tube and photodiode parallel detection array for wideband optical spectroscopy of the breast guided by magnetic resonance imaging, J Biomed Opt 19(1) (2014) 011010.

[75] B. Meng, M.R. Folaron, R.R. Strawbridge, N. Sadeghipour, K.S. Samkoe, K. Tichauer, S.C. Davis, Noninvasive imaging of dual-agent uptake in glioma and normal tissue using MRI-coupled fluorescence tomography, Optical Tomography and Spectroscopy of Tissue XIII, International Society for Optics and Photonics, 2019, p. 1087413.

[76] S.C. Davis, K.S. Samkoe, K.M. Tichauer, K.J. Sexton, J.R. Gunn, S.J. Deharvengt, T. Hasan, B.W. Pogue, Dynamic dual-tracer MRI-guided fluorescence tomography to quantify receptor density in vivo, Proceedings of the National Academy of Sciences 110(22) (2013) 9025-9030.

[77] S.C. Davis, K.S. Samkoe, J.A. O'Hara, S.L. Gibbs-Strauss, H.L. Payne, P.J. Hoopes, K.D. Paulsen, B.W. Pogue, MRI-coupled fluorescence tomography quantifies EGFR activity in brain tumors, Acad Radiol 17(3) (2010) 271-6.

[78] F. Leblond, S.C. Davis, P.A. Valdes, B.W. Pogue, Pre-clinical whole-body fluorescence imaging: Review of instruments, methods and applications, J Photochem Photobiol B 98(1) (2010) 77-94.

[79] S.C. Davis, B.W. Pogue, R. Springett, C. Leussler, P. Mazurkewitz, S.B. Tuttle, S.L. Gibbs-Strauss, S.S. Jiang, H. Dehghani, K.D. Paulsen, Magnetic resonance--coupled fluorescence tomography scanner for molecular imaging of tissue, Review of Scientific Instruments 79(6) (2008) 064302-10.

[80] S.C. Davis, H. Dehghani, J. Wang, S. Jiang, B.W. Pogue, K.D. Paulsen, Image-guided diffuse optical fluorescence tomography implemented with Laplacian-type regularization, Opt Express 15(7) (2007) 4066-82.

[81] F. Nouizi, J. Brooks, D.M. Zuro, S.K. Hui, G. Gulsen, Development of a theranostic preclinical fluorescence molecular tomography/cone beam CT-guided irradiator platform, Biomedical Optics Express 13(11) (2022) 6100-6112.

[82] F. Nouizi, J. Brooks, D.M. Zuro, S.S. Madabushi, D. Moreira, M. Kortylewski, J. Froelich, L.M. Su, G. Gulsen, S.K. Hui, Automated in vivo Assessment of Vascular Response to Radiation using a Hybrid Theranostic X-ray Irradiator/Fluorescence Molecular Imaging System, IEEE Access  (2020).

[83] Y. Lin, Temperature modulated fluorescence tomography in a  turbid media   Applied Physics Letters, 2012.

[84] M. Mehrabi, F. Nouizi, M. Algarawi, T.C. Kwong, H. Erkol, U. Sampathkumaran, G. Gulsen, CCD-based temperature modulated fluorescence tomography, Optical Tomography and Spectroscopy of Tissue XIII, International Society for Optics and Photonics, 2019, p. 108740Y.

[85] F. Nouizi, T. Kwong, Y. Lin, U. Sampathkumaran, A. Shaaz, G. Gulsen, A combined HIFU-Fluorescence Tomography high-resolution imaging technique using temperature-modulated thermodots, Optical Trapping Applications, Optical Society of America, 2013, p. JW3B. 8.

[86] Y. Lin, T.C. Kwong, L. Bolisay, G. Gulsen, Temperature-modulated fluorescence tomography based on both concentration and lifetime contrast, J Biomed Opt 17(5) (2012) 056007.

[87] Y. Lin, L. Bolisay, M. Ghijsen, T.C. Kwong, G. Gulsen, Temperature-modulated fluorescence tomography in a turbid media, Appl Phys Lett 100(7) (2012) 73702-737024.